Weld Properties of AISI 303 Free-Machining Stainless Steel

Tests identify the most appropriate composition ranges for strength, ductility, and welding response

BY J. A. BROOKS, S. H. GOODS, AND C. V. ROBINO

ABSTRACT. The all-weld-metal tensile properties from gas tungsten arc and electron beam welds, as well as shear properties of pulsed laser beam welds, have been determined for a free-machining austenitic stainless steel. Ten heats with sulfur contents from 0.04 to 0.4 wt-% and a wide range of Cr_{eq}/Ni_{eq} ratios were studied. Tensile properties of welds with both gas tungsten arc and electron beam processes were related to alloy composition and solidification microstructure. The yield and ultimate tensile strength increased with increasing Cr_{eq}/Ni_{eq} ratio and ferrite content, whereas the ductility, as measured by reduction of area at fracture, decreased with sulfur content. Similar behavior was observed for the shear behavior of the pulsed laser beam welds. A range in alloy compositions was identified that provided a good combination of both strength and ductility. The solidification cracking response for the same range of compositions is discussed, and compositions identified that would be expected to provide good performance in welded applications.

Introduction

Austenitic stainless steels are used in a wide range of applications, often because of their good corrosion resistance, mechanical behavior, and magnetic properties. However, because of their high work-hardening rate, toughness, and ductility, these materials are known to be difficult to machine. In general, tools run hotter with more tendency to form buildup at the tool edge, chips are stringier with the tendency to tangle, tool chatter can be exacerbated, and feed rate can be more critical than with other materials. The use of free-machining grades can greatly reduce machining time and improve surface quality. Commonly, the free-machining grades are alloyed with small amounts of low solubility elements such as sulfur, lead, and selenium. These elements aid machinability by forming precipitates or inclusions that cause the chip to break into short fragments instead of continuing as lengthy turnings. Also, the inclusions appear to help lubricate the tip of the tool at the cutting edge, thereby minimizing galling and seizing.

Free-machining stainless steels have seen little use in applications involving welding. The two concerns restricting their use are weld hot cracking and uncertainties in weld mechanical properties. However, it has been shown for AISI 303, the most widely used free-machining grade (alloyed with sulfur), that if the welds solidify as primary ferrite they can be very resistant to cracking (Refs. 1–4).

For gas tungsten arc (GTA) welds, the critical Cr_{eq}/Ni_{eq} ratio for primary ferrite solidification was found (Refs. 3, 4), when using Hammar and Svensson equivalents (Ref. 5), to be in the range of 1.55 to 1.6. For pulsed laser beam welds, the critical value was found to increase to ~1.75 (Refs. 3, 4). In essence, this increase is due to the fact that higher Cr_{eq}/Ni_{eq} ratios are required to maintain ferritic solidification at higher solidification velocities (dendrite tip undercooling increases more rapidly with increasing solidification velocity during ferritic solidification than during austenitic solidification (Refs. 6–12).

It was also shown in Ref. 4 that at higher sulfur levels, the transition in solidification mode appeared to be shifted to slightly higher Cr_{eq}/Ni_{eq} ratios. Moreover, it was observed for GTA welds that solidification cracking susceptibility increased for Cr_{eq}/Ni_{eq} ratios above ~1.9. It should also be noted that the heats studied contained a high level of phosphorous that is also known to promote cracking (Refs. 13–16). Nevertheless, for high levels of sulfur, a range in compositions with Cr_{eq}/Ni_{eq} ratios between ~1.7 and 1.9 showed good welding behavior for both GTA and laser welding processes. These two processes cover an extremely wide range of solidification velocities.

The second area of concern with high sulfur levels is the lack of information regarding weld mechanical properties. The presence of solidification cracks could certainly have a catastrophic effect on weld strength and ductility. However, in the absence of solidification defects, the presence of Mn- and Cr- containing sulfides may, in themselves, be expected to have an adverse affect on weld properties. A goal of this study was to determine the effects of sulfur content and Cr_{eq}/Ni_{eq} ratio on all-weld-metal tensile properties of crack-free GTA and EB welds. The alloys used to study mechanical properties were identical to those used in the earlier solidification and cracking studies (Ref. 3, 4).

KEY WORDS

Free Machining
Stainless Steels
Gas Tungsten Arc Welding
Electron Beam Welding
Laser Beam Welding
Sulfur
Weld Properties

Materials and Experimental Procedures

The chromium and nickel contents were adjusted to provide a range of Cr_{eq}/Ni_{eq} ratios in ten experimental vacuum induction melted heats of AISI 303 stainless steel. The 11-kg cast ingots were homogenized and hot rolled into strips ~7.6 cm wide and 3.2 mm thick. As can be seen in Table 1, all other alloying elements were held constant except for sulfur, which was varied from 0.04 to 0.4 wt-%. Phosphorus, an impurity known to promote solidification cracking, was held at the maximum allowable level of 0.03 wt-% and should therefore represent a worst case for cracking. Table 1 also includes the Cr_{eq}/Ni_{eq} ratios calculated using the equivalents of both Hammar and Svensson (Ref. 5) and the WRC 92 diagram (Ref. 17). It can be seen the Cr_{eq}/Ni_{eq} ra-

J. A. BROOKS and S. H. GOODS are with Sandia National Laboratories, Livermore, Calif., and C. V. ROBINO is with Sandia in Albuquerque, N.Mex.

tios range from 1.55 to 1.94. The ferrite numbers (FN) shown in Table 1 are those calculated using the WRC 92 diagram and are very similar to those calculated using the DeLong diagram (Ref. 18).

Longitudinal all-weld-metal GTA tensile specimens were made from 3.2-mm-thick plates welded from each side to produce full-penetration welds that were approximately 6 mm wide at the surface. The welds were made using 120 A, 9.3 V with Ar shielding at a travel speed of 3 mm/s. Flat dogbone tensile specimens machined from these welds were 1.3 mm thick and had a reduced gauge section 3.2 mm wide and 19 mm long. Electron beam welds made from the same plate material were also butt joint welded from each side. Welds were made at 25.4 mm/s using 130 kV and 32 mA with circular deflection and a defocused beam. Flat tensile specimens used for the all-weld-metal EB tensile properties were 2.54 mm wide and 1.27 mm thick. Samples were tested using a noncontacting laser extensometer at an initial strain rate of 0.005/s.

In addition to GTA and EB welds, it was desired to determine the effect of microstructure and sulfur content on properties of pulsed laser beam welds. However, since standardized test techniques do not exist for small single-pulse welds, a shear-type test was used to determine the relative performance of the ten experimental heats. The welds were produced using a Nd:YAG laser operating at 3.7 J/pulse, which resulted in welds with a cross-sectional area of approximately 1.75 mm^2 in the plane of the joint. The welds were shear tested using the configuration shown in Fig. 1 with a crosshead speed of 0.043 mm/s and a stand-off (gauge length) of 0.075 mm. Weld cross-sectional area in the shearing plane was measured metallographically on separate welds and was taken as the average of five measurements.

GTA Weld Results

The GTA weld microstructures corresponded closely to those expected from consideration of the Cr_{eq}/Ni_{eq} ratios (Refs. 19–23). A schematic of the solidification behavior and idealized microstructures is shown in Fig. 2 with Cr_{eq}/Ni_{eq} ratio increasing from left to right. The two schematic representations at the left of the figure correspond to primary austenite solidification, with the one at the higher ratio depicting solidification with some eutectic ferrite (austenite/ferrite solidification, A/F). Three primary ferrite solidified structures are shown at the right side of the figure. (It has been reported the two microstructures shown to solidify as F/A may also form in single-phase ferrite-solidified structures where the transformation to austenite occurs shortly after solidification (Refs. 24, 25).) The change in solidification mode from primary austenite to primary ferrite increases with increasing solidification velocity, but for typical GTA welds occurs at a $Cr_{eq}/Ni_{eq.}$ ratio of ~1.5 (Hammar and Svensson equivalents) (Refs. 19–21, 26). However, it should be noted welds often contain several of the adjacent microstructures shown in the schematic of Fig. 2.

The heats with a Cr_{eq}/Ni_{eq} ratio of 1.55 solidified in a mixed mode, with some regions of primary austenite with eutectic ferrite, and others as primary ferrite with skeletal ferrite (F/A). This Cr_{eq}/Ni_{eq} ratio is close to that where the transition in solidification mode is commonly believed to change from primary austenite to primary

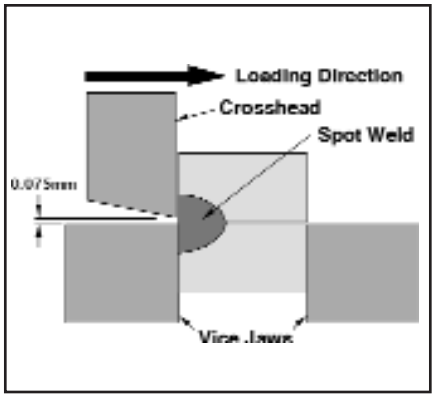

Fig. 1 — Schematic diagram of laser beam spot weld shear test.

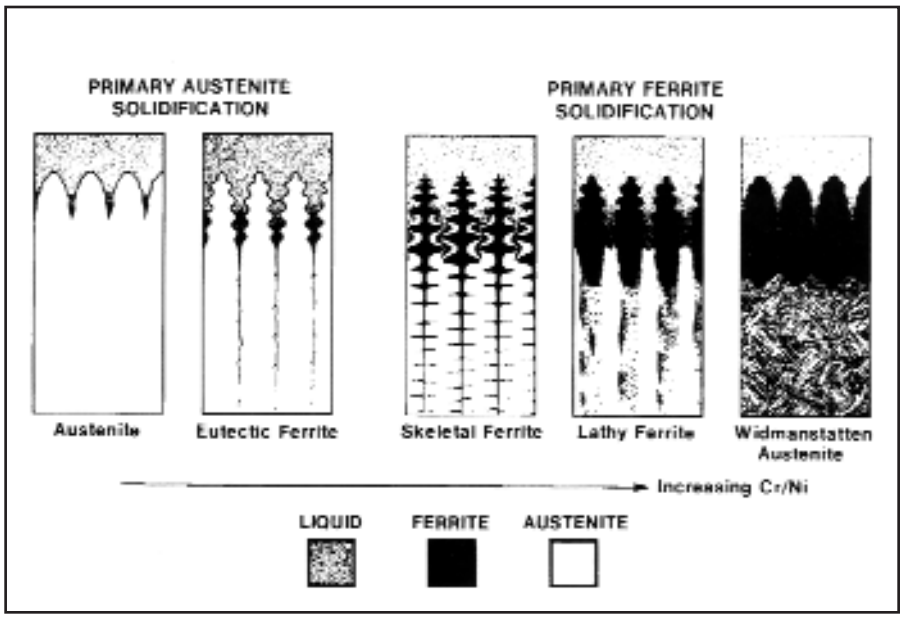

Fig. 2 — Schematic of weld solidification and solid-state transformation behavior shown for increasing Cr_{eq}/Ni_{eq} ratio.

Table 1 — Alloy Compositions (wt-%), Calculated Cr_{eq}/Ni_{eq} Ratios, and Ferrite Numbers (FN)

Heat No.	1	2	3	4	5	6	7	8	9	10
S	0.04	0.04	0.04	0.11	0.27	0.42	0.11	0.12	0.27	0.18
Cr	17.55	19.18	18.37	18.45	18.47	18.45	16.87	17.78	17.77	18.16
Ni	10.51	8.92	9.73	8.60	8.49	8.61	10.08	9.29	9.30	8.83
C	0.03	0.03	0.03	0.03	0.03	0.03	0.03	0.03	0.03	0.03
Mn	1.48	1.49	1.48	1.49	1.48	1.48	1.47	1.48	1.49	1.47
Si	0.62	0.59	0.62	0.61	0.57	0.57	0.59	0.61	0.59	0.61
P	0.03	0.03	0.03	0.03	0.03	0.03	0.03	0.03	0.03	0.03
Mo	0.35	0.35	0.35	0.35	0.35	0.35	0.35	0.35	0.35	0.35
Cu	0.31	0.30	0.30	0.30	0.30	0.30	0.30	0.31	0.30	0.30
N	0.02	0.02	0.02	0.02	0.02	0.02	0.02	0.02	0.02	0.02
Cr_{eq}/Ni_{eq} (WRC92)	1.48	1.89	1.67	1.85	1.87	1.85	1.48	1.67	1.67	1.78
Cr_{eq}/Ni_{eq} H and S	1.55	1.95	1.73	1.92	1.94	1.92	1.55	1.74	1.74	1.85
FN (WRC92)	2	14	10	12	12	12	1.5	6	6	9

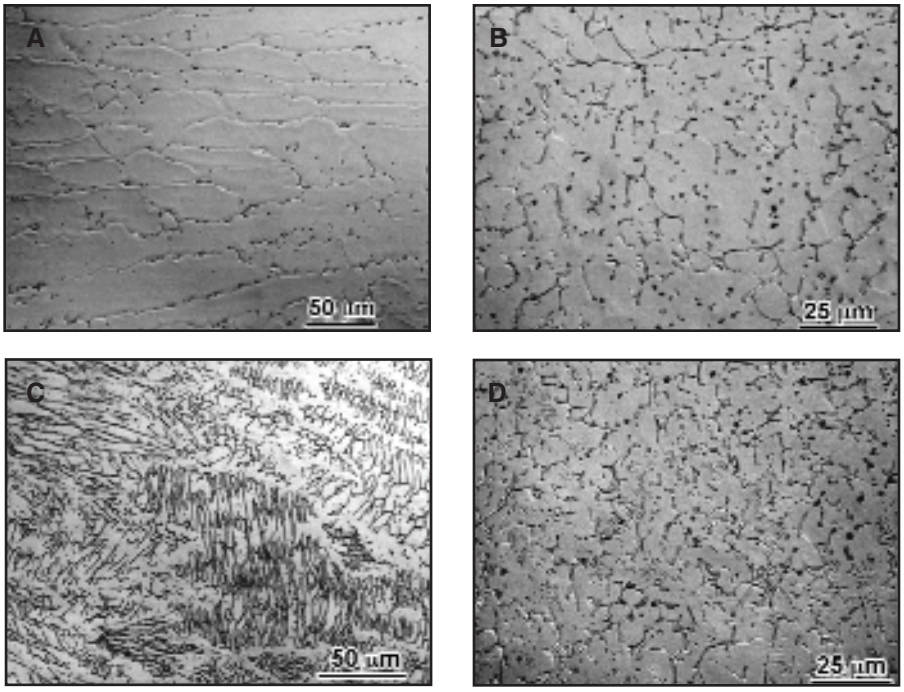

Fig. 3 — Microstructure of GTA welds. A — Heat 7, Cr_{eq}/Ni_{eq}=1.55, S=0.11 wt-%; B — Heat 9, Cr_{eq}/Ni_{eq}=1.74, S=0.27 wt-%; C — Heat 2, Cr_{eq}/Ni_{eq} = 1.95, S=0.04 wt-%; D — Heat 6, Cr_{eq}/Ni_{eq}=1.92, S=0.42 wt-%.

ferrite (Refs. 19–21). However, in general, it was found the two heats solidified somewhat differently. Heat 7 with the higher sulfur content, 0.11 wt-%, solidified largely as primary austenite while Heat 1 with 0.04 wt-% sulfur solidified largely as primary ferrite.

The microstructure of Heat 7 is shown in Fig. 3A and is characteristic of primary austenite solidification in which a small amount of eutectic ferrite is contained at the solidification cell and grain boundaries (austenite/ferrite solidification — Fig. 2). Large numbers of sulfide inclusions are also present and confined to the solidification boundaries. Scanning electron microscopy (SEM) with energy dispersive spectrometry (EDS) analysis showed the sulfides contain manganese with smaller amounts of chromium.

The weld microstructure of Heat 9 with a sulfur content of 0.27 wt-% shown in Fig. 3B is characteristic of welds with Cr_{eq}/Ni_{eq} ratios of ~1.7. The primary ferrite solidified weld (F/A) exhibits a skeletal ferrite morphology. However, at this Cr_{eq}/Ni_{eq} ratio, some regions of lathy ferrite (Fig. 2) were also observed. Large amounts of sulfides are again present both along the solidification cell boundaries as well as along ferrite austenite interphase boundaries. This primary ferrite skeletal structure is similar to the primary ferrite solidified regions of the welds with the Cr_{eq}/Ni_{eq} ratio of 1.55. It appears the high sulfur content prompted F/A vs. F solidification (Refs. 3, 4).

The final weld microstructures, Fig. 3C and D, are those from heats with the highest Cr_{eq}/Ni_{eq} ratio of ~1.9. The microstructure of Heat 2 with a Cr_{eq}/Ni_{eq} ratio of 1.95 and a sulfur content of 0.04 wt-% is shown in Fig 3C. This weld exhibits primarily a lathy ferrite structure where in some regions it is evident the laths extend over several solidification cells, which suggests that solidification occurred completely as ferrite (Refs. 19-20). In other regions where the ferrite laths are confined to the cell boundaries, solidification likely occurred as F/A. Small sulfide particles are present at both intradendritic ferrite/austenite boundaries and within the solidification boundaries. The presence of intracellular sulfides indicates that, unlike primary austenite solidification, some of the liquid sulfides are trapped during ferrite solidification rather than rejected to the cell boundaries.

The weld microstructure of Heat 6 with a Cr_{eq}/Ni_{eq} of 1.92 and the highest sulfur content, 0.42 wt-%, is shown in Fig 3D. Large quantities of sulfides are present along both the solidification cell boundaries and the ferrite austenite interphase boundaries. However, clusters of finer sulfide particles at the interdendritic regions are also present at this high sulfur content.

Longitudinal all-weld-metal GTA tensile properties are given in Table 2. The yield and ultimate tensile strengths, uniform and total elongation, and reduction in area at fracture (RA) are shown along with Cr_{eq}/Ni_{eq} ratio and sulfur content and are the average of two tests per heat. In most cases, the variation in tensile strengths between the two tests were within a few percent. However, variations in ductility were higher, in several cases as high as 10% relative. The graphic representation of the data in Fig. 4 shows the correlation between strength and FN. It can be seen an increase in calculated FN from 2 to ~12 resulted in a ~25% increase in YS and a 15% increase in UTS.

The tensile ductility measured as uniform elongation and %-RA is plotted as a function of sulfur level in Fig. 5. It can be seen the elongation is in the range of 40–50% for sulfur levels below 0.3% and above 35% at the highest level tested. As can be seen in Table 2, the total elongation in most cases was not much greater than the uniform elongation, indicating only a small amount of necking occurred in the specimens prior to fracture. The %-RA shows a stronger and more systematic sulfur dependence, with measured %-RA decreasing from ~55% at the lowest level of sulfur to less than 30% at 0.42 wt-%. This behavior is summarized in Fig. 6, which shows the strong correlation between strain after uniform elongation (ε_t-ε_u) and RA.

The weld fracture surfaces were analyzed using SEM to determine the influence of microstructure on fracture. The results of these evaluations are shown in Fig. 7A–C for welds with sulfur contents of 0.04, 0.27, and 0.42 wt-%. In all cases, fracture occurred by microvoid coalescence where the microvoids initiated at second-phase (primarily sulfide) particles.

EB Weld Results

The EB weld microstructures were similar to those of the GTA welds of the same composition. The primary difference was that the EB welds exhibited a finer structure due to the higher solidification velocity and cooling rates. The primary austenite solidified microstructure of Heat 7, Fig. 8A, is characteristic of both heats with the Cr_{eq}/Ni_{eq} ratio of 1.55. Unlike the GTA welds, little eutectic ferrite and no regions of primary ferrite were observed. It can be seen all sulfides are again confined to the solidification boundaries. The microstructure of heats with a Cr_{eq}/Ni_{eq} ratio of 1.74 exhibited mainly skeletal ferrite. This is shown in Fig. 8B for Heat 9. It is also very evident with the primary ferrite solidified structure the sulfides are not confined to the cell boundaries alone, and a fraction are also trapped within the intradendritic regions. This observation again demonstrates the differences between the two different solidification modes in terms of sulfide trapping at the solid-liquid interface.

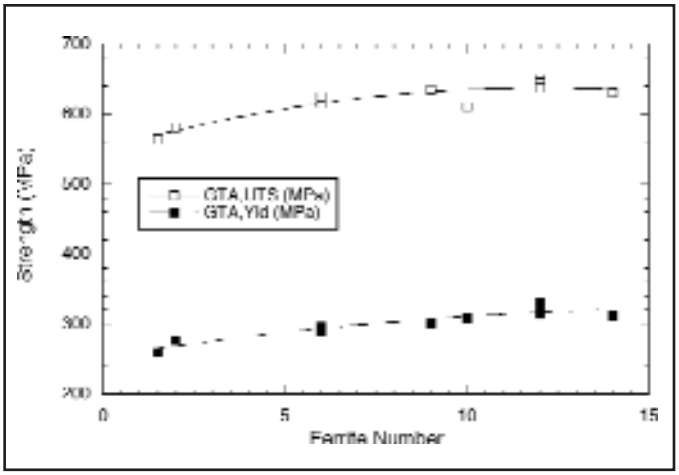

Fig. 4 — Yield and tensile strength vs. calculated FN for GTA all-weld-metal tensile samples.

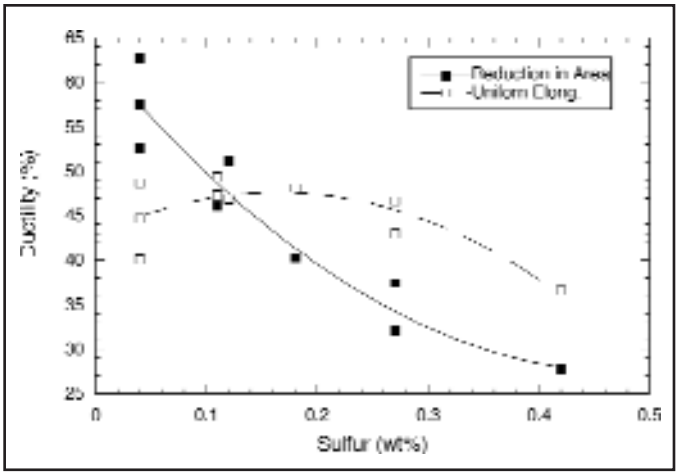

Fig. 5 — Uniform elongation and reduction in area vs. sulfur content of all-weld-metal GTA tensile samples.

The welds with the highest Cr_{eq}/Ni_{eq} ratios (~1.94) solidified as primary ferrite and exhibited a mixture of skeletal and lathy ferrite — Fig. 8C.

The EB all-weld-metal tensile properties are given in Table 3. Again the results are averages of two tests per heat (except for Heats 7 and 10). Like the GTA welds, in most cases variations in tensile strengths between the two tests were within a few percent, while variations in ductility were as high as 10% in some cases. However, one of the Heat 7 specimens exhibited both low strength and low ductility, only a little over 10% elongation. This sample also exhibited large amounts of secondary cracking along the gauge length. SEM examination of fracture surfaces of this specimen, and both specimens from Heat 1, showed evidence of prior solidification cracks. The tensile properties were therefore controlled largely by weld defects, the solidification cracks, rather than the weld microstructure. Thus the data in Table 3 for Heat 1 is characteristic of welds with these defects. The results from the one Heat 7 specimen were not included in the data in Table 3. The EB tensile strengths plotted for all the weld heats except for Heat 1 are shown in Fig. 9 along with the GTA weld data. It can be seen that similar to the GTA welds, both the yield and tensile strengths increase with FN. The ductility, plotted as %-RA vs. sulfur content, is shown in Fig. 10. Again, there is a strong correlation between fracture behavior and sulfur content and the behavior is similar for both processes, although the ductility of the EB welds is slightly lower on average.

The EB weld fracture surfaces were also examined by electron microscopy. The welds from Heat 1 with a Cr_{eq}/Ni_{eq} ratio of 1.55 and 0.04 wt-% sulfur and which exhibited both low strength and ductility were of special interest. Figure 11A shows at low magnification the weld fracture that exhibits a very prominent, flat-appearing region on the upper left side of the fracture surface. Higher magnification, Fig. 11B, shows this region exhibits a smooth columnar appearance characteristic of a solidification crack with evidence of fine surface porosity. Also, transverse to the solidification direction were sulfides associated with the solidification crack that had a rather unusual stringer morphology. A region near the center of the specimen is shown in Fig.

Table 2 — All-Weld-Metal GTA Tensile Properties

Heat No.	Cr_{eq}/Ni_{eq}	S (wt-%)	Ys (MPa)	UTS (MPa)	ε_u (%)	ε_T (%)	$\varepsilon_T-\varepsilon_u$	R A (%)
1	1.55	0.04	276.3	581.2	48.7	51.1	2.4	53
2	1.95	0.04	312.5	630.4	40.2	44.6	4.4	63
3	1.73	0.04	308.7	610.4	44.7	47.8	3.1	58
4	1.92	0.11	313.8	651.1	47.2	50.0	2.8	46
5	1.94	0.27	329.3	645.2	43.0	43.3	0.3	32
6	1.92	0.42	324.5	637.7	36.6	36.7	0.1	28
7	1.55	0.11	259.8	564.3	49.3	50.5	1.2	47
8	1.74	0.12	289.4	613.9	46.8	49.5	2.7	51
9	1.74	0.27	296.3	624.6	46.6	47.7	1.1	37
10	1.85	0.18	300.6	634.6	47.7	48.2	0.5	40

Table 3 — All-Weld-Metal Electron Beam Tensile Properties

Heat No.	Cr_{eq}/Ni_{eq}	S (wt-%)	YS (MPa)	UTS (MPa)	ε_u (%)	ε_T (%)	RA (%)
1[a]	1.55	0.04	253	413	16.1	16.6	
2	1.95	0.04	339	645	41.2	48.2	57
3	1.73	0.04	306	577	40.8	47.7	54
4	1.92	0.11	338	654	43.4	46.9	41
5	1.94	0.27	352	643	31.9	32.0	24
6	1.92	0.42	373	635	28.6	28.7	21
7	1.55	0.11	330	532	50.3	50.5	41
8	1.74	0.12	303	595	43.0	48.6	44
9	1.74	0.27	304	604	44.1	44.2	30
10	1.85	0.18	341	654	42.4	42.7	29

(a) Properties reflect presence of solidification cracks.

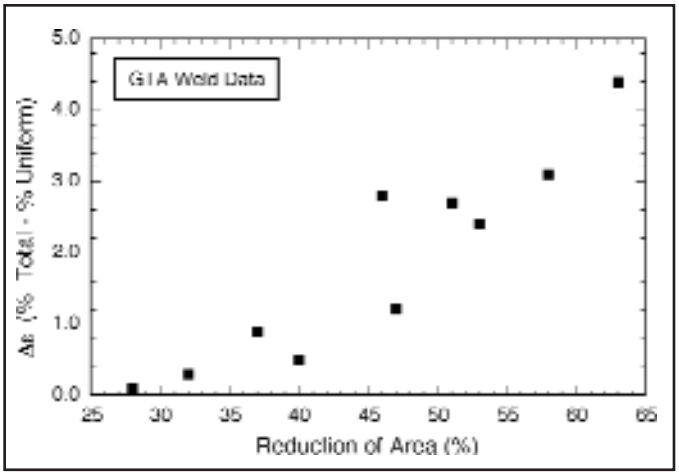

Fig. 6 — GTA weld Δε (% total elongation - % uniform elongation) vs. % reduction in area at fracture.

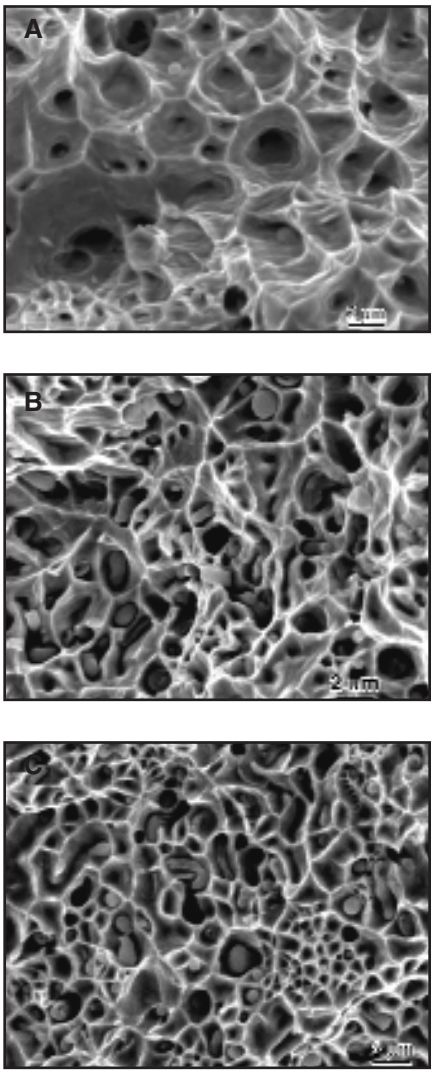

Fig. 7 — GTA tensile fracture surfaces at A — sulfur level of 0.04 wt-% (Heat 2); B — sulfur level of 0.27 wt-% (Heat 9); and C — sulfur level of 0.42 wt-% (Heat 6). Note fracture initiated at second-phase Mn- and Cr- containing sulfides.

11C. In this location, the fracture surface exhibits a prominent columnar appearance, with a finer scale ductile rupture. Thus, the low strength and ductility of these welds can be attributed to preexisting solidification cracks. It can be seen in Fig. 11A that a large amount of necking had occurred prior to premature failure resulting from the large defect. A similar but smaller solidification crack region was observed in one of the welds of Heat 7, which again resulted in poor weld properties. As noted above, the results from this specimen were not included in the data plotted in Figs. 9 and 10.

In general, the fracture appearance of all the EB specimens at low magnification exhibited a columnar dendritic appearance similar to that shown in Fig. 11C. Furthermore, in all cases, the fracture occurred by a ductile process with nucleation and growth of voids at sulfide particles. It was found that as the sulfur content increased, the size and area fraction of sulfides on the fracture increased. This observation is shown in Fig. 12 for sulfur contents of 0.04, 0.11, and 0.42 wt-%. Figure 12A shows that at the lowest sulfur concentration (0.04 wt-%), the large majority of sulfides are spherical in shape and approximately 0.5 to 1 μm in diameter. It is clearly evident that fracture initiated at these particles. At a higher sulfur content (0.11 wt-%), Fig. 12B, a larger number of particles are evident, along with the accompanying smaller average dimple size. It can also be seen that some agglomeration of sulfides has occurred to form larger elongated particles. However, the majority of the sulfides remain spherical but slightly larger than observed at lower S levels. Figure 12C shows the sulfide morphology was significantly different at the highest level of sulfur, 0.42 wt-%. Here, in addition to a few large, nearly spherical sulfides, a large number of agglomerated and elongated sulfides are also present. In addition, there are also numerous colonies of very fine spherical sulfides. It should be noted the heat shown in Fig. 12C has one of the highest Cr_{eq}/Ni_{eq} ratios.

Single-Pulse Laser Beam Welds

The microstructures of the laser beam welds have been reported in detail elsewhere (Ref. 4). In general, they could be separated into three groups, dependent upon Cr_{eq}/Ni_{eq} ratio. The two heats with the Cr_{eq}/Ni_{eq} of 1.55 and Heat 9 with a Cr_{eq}/Ni_{eq} of 1.74, but with the highest sulfur content, S=0.27%, solidified as 100% austenite. The other two heats with a Cr_{eq}/Ni_{eq} of 1.74 solidified in a mixed mode, some regions as primary ferrite and others as primary austenite. The remainder of the heats with the higher Cr_{eq}/Ni_{eq} ratios solidified as single-phase ferrite. It was believed the primary ferrite massively transformed to austenite on cooling, leaving all the welds completely austenitic with no ferrite.

The results of the shear tests on the laser beam spot welds are given in Fig. 13. Although there is significant variability in the measured spot weld strength, there appears to be little if any dependence of strength on Cr_{eq}/Ni_{eq} (or calculated FN). Note all welds are ferrite free. In the case of the spot welds, the lower strength of Heat 1 may be attributable to the presence of solidification cracks in the primary austenite structure. This data point was not considered when determining the dependence of strength on Cr_{eq}/Ni_{eq}, ratio in Fig 13. It is interesting that lower strength was not apparent in welds in the other heat (Heat 7) with the same low Cr_{eq}/Ni_{eq} ratio of 1.55, in which cracks were also expected. Scatter in the tests can be due to a variety of other sources, such as hinging during loading, but, in general, the strength levels for these welds are similar and independent of sulfur content. Observation of the fracture surfaces indicated ductile failure for all heats.

The compliance of the load train in the shear test apparatus prevented the direct determination of shear strain at failure of the spot weld. However, since the load (strength) levels for all alloys tested are similar, a comparative measure of the ductility can be obtained from the time to failure for each of the tests. This comparison is shown in Fig. 13B, which plots time to failure as a function of sulfur level. The results are analogous to ductility measurements of the GTA and EB welds and display similar trends. In general, there is a reduction in strain to failure at high sulfur levels, although the relative decrease is lower for the shearing tests than the ductilities measured in the tensile tests of the other weld types. Given the size of the welds and the relatively high loading rate, the failure times imply these welds are likely acceptable for many applications.

Discussion

The GTA yield and tensile strengths shown in Fig. 4 increased 25% and 15%, respectively, with an increase in calculated

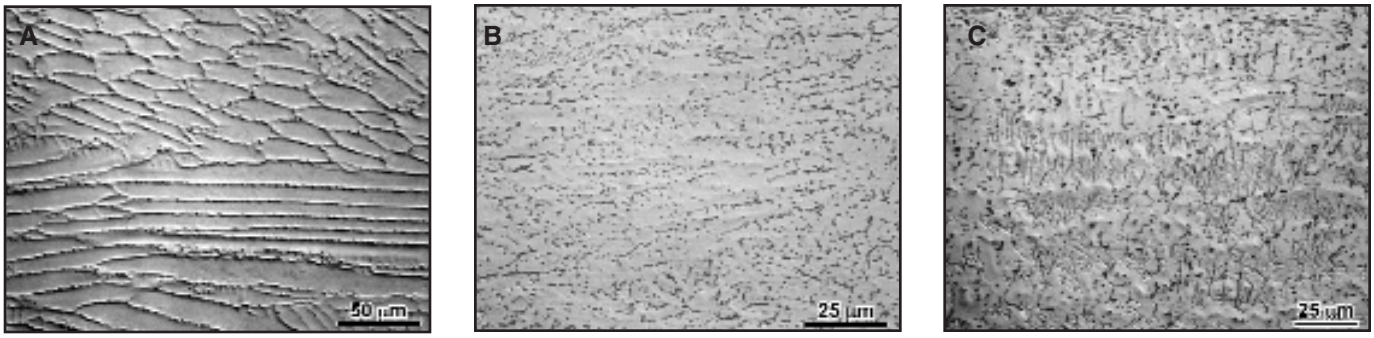

Fig. 8 — Microstructures of EB welds. A — Heat 7, Cr_{eq}/Ni_{eq}=1.55, S=0.11 wt-%; B — Heat 9, Cr_{eq}/Ni_{eq}=1.74, S=0.27 wt-%; C — Heat 6, Cr_{eq}/Ni_{eq}=1.92, S=0.42 wt-%.

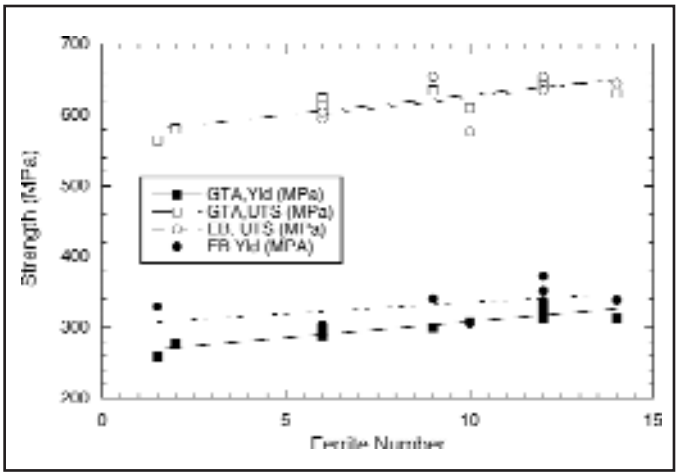

Fig. 9 — Comparison of EB and GTA yield and tensile strengths vs. calculated ferrite number.

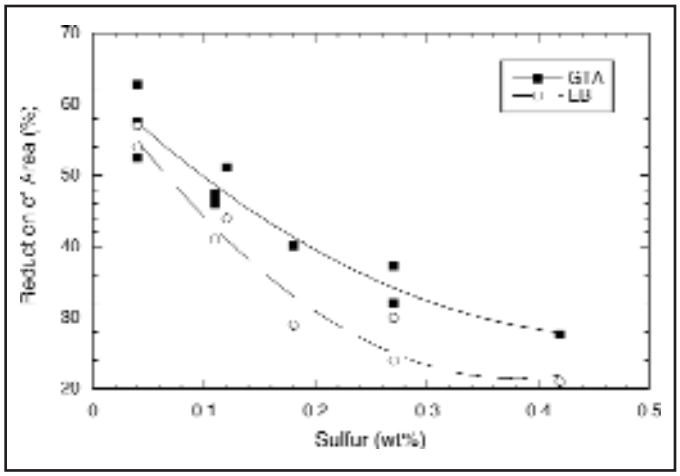

Fig. 10 — Reduction in area at fracture of EB and GTA welds vs. sulfur content.

FN from ~2 to 12. For the range in FN studied here, FN and %-ferrite are similar in value. Thus it appears the increase in strength can be attributed largely to the presence of the second phase. Although there were a large number of sulfide particles, their rather large size does not appear to result in significant strengthening.

The ductilities of the GTA welds are plotted vs. sulfur content in Fig. 5. At the low S levels, 0.04 wt-%, there is a range in RA and uniform elongation of ~20% between heats with the three different Cr_{eq}/Ni_{eq} ratios (Table 2). This range in ductilities may be largely attributed to scatter in the test results. Note there is no consistent correlation in ductility of these heats. The heat with the highest uniform elongation, Heat 1, has the lowest RA, whereas the heat with the lowest uniform elongation, Heat 2, has the highest RA. However, since uniform elongation is largely dependent on strain hardening, and RA is determined primarily by microvoid coalescence, they are not necessarily related.

In general, sulfur did have a large effect on ductility (Fig. 5), reducing the RA from ~60% at the lowest sulfur level to 32% at the highest sulfur level independent of Cr_{eq}/Ni_{eq} ratio. There was also a significant decrease in elongation at the very highest level of sulfur, 0.42 wt-%. In cases where there were no preexisting weld defects, it was found fracture occurred by microvoid initiation and coalescence. The void initiation occurred at sulfide particles that were primarily concentrated along solidification boundaries, resulting in a columnar dendritic fracture appearance. The reduction in ductility with increasing sulfur content can be attributed to a higher number and size of fracture initiation sites that facilitate the ductile fracture process. The reduction of dimple size with increasing sulfur content is apparent in the fractographs in Fig. 7. It can be seen in Fig. 7C that the clusters of fine sulfide particles, which are also evident in the optical micrograph in Fig. 3D, play a major role in fracture behavior at the highest sulfur level. The acceleration of microvoid coalescence processes with increasing sulfur content also results in the reduction in elongation after the onset of necking. This is largely responsible for the relationship between RA and $\Delta\varepsilon$ ($\varepsilon_t - \varepsilon_u$) in Fig. 6. However, it is important to note that even for sulfur levels as high as ~0.3 wt-%, the welds still exhibit a good combination of strength and ductility (uniform elongation more than ~40%).

It might be expected that weld microstructure also influences the effect of sulfur on fracture behavior. In the primary austenite solidified heats, the sulfides are more confined to the solidification cell boundaries, which reduces particle spacing along the fracture path. Furthermore, due to the lower solidification partitioning coefficient and lower solubility of sulfur in austenite than in ferrite, these heats may also be expected to have a slightly higher sulfide content for the same sulfur level, for example, Heat 1 vs. Heat 3. These factors would have a tendency to reduce RA in these welds compared to primary ferrite solidified structures of the same sulfur content. However, a more detailed study is required to determine the effect, if any, of weld microstructure/sulfur interactions on fracture behavior.

The EB welds exhibited mechanical behavior similar to the GTA welds. The primary difference was attributed to solidification cracking that occurred in the

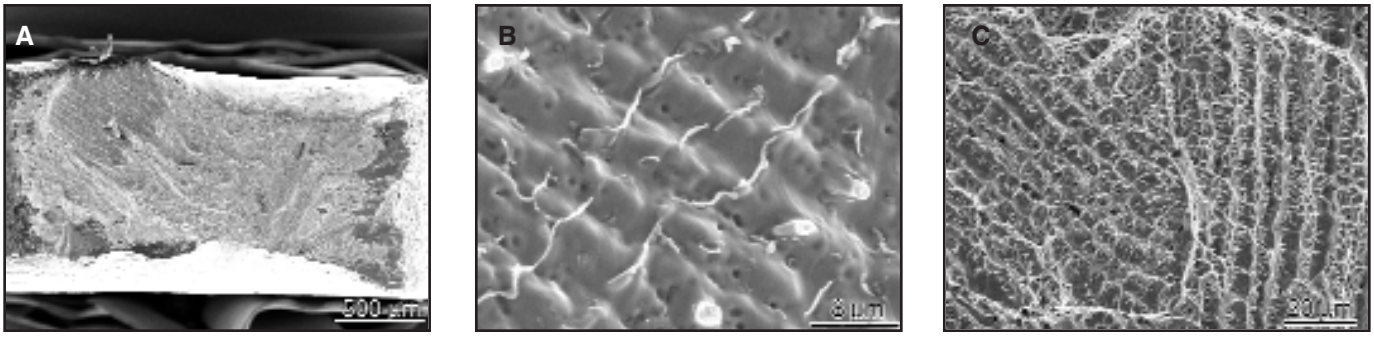

Fig. 11 — SEM images of the fracture surface of the EB tensile specimen of Heat 1. A — Low magnification showing crack on the upper left of the fracture surface; B — higher magnification of solidification crack surface showing sulfide stringers transverse to the solidification direction; C — fracture surface at center of specimen exhibiting a columnar structure and underlying ductile fracture typical of all the specimens.

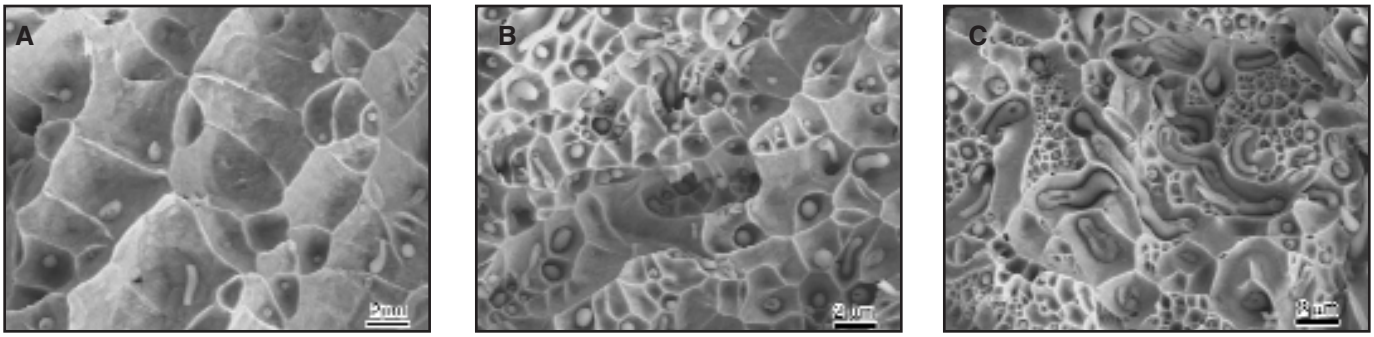

Fig. 12 — EB tensile fractures showing change in appearance with increasing sulfur content: A — Heat 1 with 0.04 wt-% S; B — Heat 7 with 0.11 wt-% S; and C — Heat 6 with 0.042 wt-% S. The fracture is seen to initiate at sulfides with a variety of sizes and morphologies.

welds with the lowest Cr_{eq}/Ni_{eq} ratio, i.e. Heat 1 and one of the specimens from Heat 7. The tensile strengths are plotted in Fig. 9. It can be seen that the measured yield strengths are similar for both processes, with those of the EB welds being perhaps slightly higher, ~10%. This increase may be due to the finer microstructure, as can be seen by comparing the microstructures in Figs. 3 and 8. It can also be seen in Fig. 9 that the yield strengths of the EB welds show less of a dependence on FN. Although FN was not measured, it appeared the ferrite content of the EB welds was less than that of the GTA welds made on the same heats. The ultimate tensile strengths of the two weld processes are very similar.

The reduction in area at fracture for both welding processes is shown in Fig 10. It can be seen that the trends are the same for both processes, with the RA decreasing with increasing sulfur content. The more precipitous decrease in RA might be expected for the EB welds since the dendrite spacing and sulfide size would both be smaller than in the GTA welds due to the higher cooling rate. This is apparent when comparing the micrographs in Figs. 3 and 8. The volume fraction of sulfides should remain nearly constant for each heat with both welding processes, except for a small reduction of sulfides in the EB welds due to higher solute trapping at the higher solidification velocities. Overall, with the finer solidification structure, the number of sulfide particles should be greater and the mean particle spacing less in the EB welds. Ductile fracture models predict in this case that the strain to fracture would decrease for the larger number of particles at the same volume fraction (Ref. 27).

The shear test results of the single-pulse laser beam welds indicated very good properties may be achieved at high sulfur levels. Similar to the EB welds, the strength of the primary austenite solidified welds reflected the presence of weld defects. Thus for high reliability welds with the high P and S levels studied here, a requirement would be that the welds solidify as ferrite. Irrespective of defects, the shear strengths of the laser beam welds plotted in Fig. 13A appear to show very little if any increase in strength at the higher Cr_{eq}/Ni_{eq} ratios. However, unlike the EB and GTA welds where ferrite appears to contribute to strengthening, the laser weld microstructures were all single-phase austenite. Any slight increase in strength may be due to the finer grain size that the higher Cr_{eq}/Ni_{eq} ratios welds exhibited as a result of the massive transformation of ferrite to austenite. The grain sizes of the primary austenite structures were considerably larger. Similar to the weld tensile tests of the GTA and EB welds, the shear tests of the laser beam welds showed an apparent loss in ductility at the highest levels of sulfur. Although the loss in ductility was not as apparent in the laser beam welds, the loss may be more significant under other (e.g., tensile) loading conditions. Nevertheless, it appears acceptable strength and ductility can be achieved at sulfur levels as high as 0.25% for all three welding processes.

The observation of cracks in the HED welds with a Cr_{eq}/Ni_{eq} ratio of 1.55 is not unexpected for primary austenite solidification (Ref. 28). It is well known welds that solidify as primary austenite are much more susceptible to solidification cracking than welds that solidify as primary ferrite (Refs. 29–34). It is also common that welds made with the high-energy-density (HED) processes and the associated high thermal gradients are more susceptible to cracking than conventional GTA welds. It was observed here that the GTA welds with Cr_{eq}/Ni_{eq} of 1.55 solidified in a mixed mode, with the higher sulfur heat exhibiting a larger fraction of primary austenite solidification. An earlier study involving these alloys showed that, for Cr_{eq}/Ni_{eq} ratios between 1.73 and 1.90, both GTA and pulsed laser beam welds exhibited good resistance to solidification cracking. The

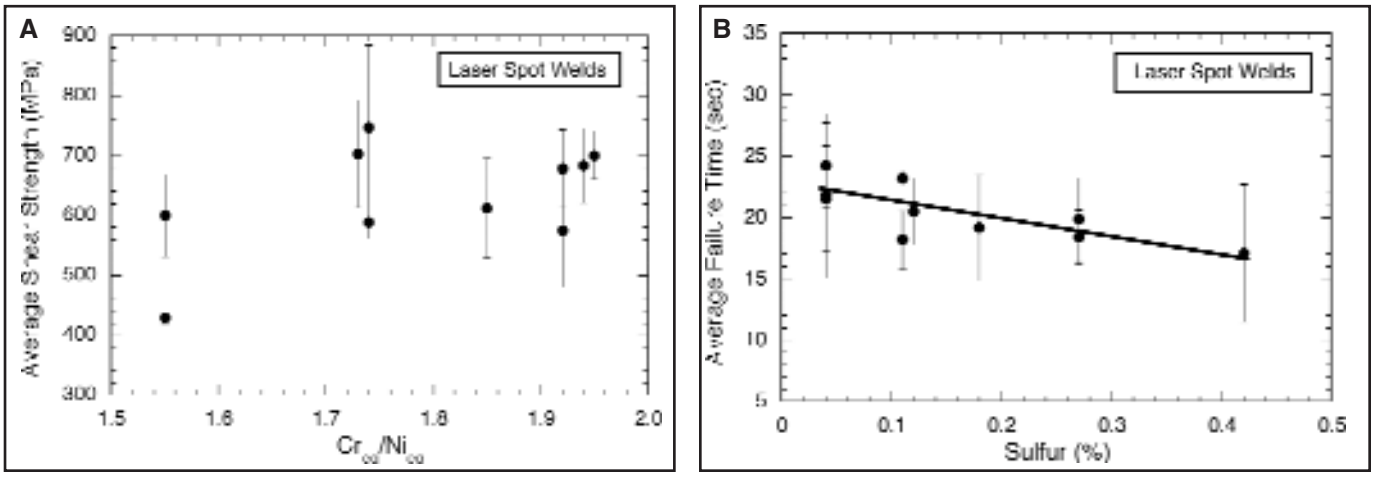

Fig. 13 — A — Average spot weld shear strength as a function of Cr_{eq}/Ni_{eq}; B — ductility plotted as time to failure during shear testing vs. sulfur content.

upper limit of Cr_{eq}/Ni_{eq} ratio was set by the GTA process and the lower limit by the high solidification rates of the pulsed laser beam welding process. These results are summarized in Fig. 14, along with data from Pacary et al. (Ref. 33) and Lienert (Ref. 34), where cracking susceptibility is plotted as (P+S) vs. Cr_{eq}/Ni_{eq} ratio (using the equivalents of Hammar and Svennson). For the intermediate solidification velocities of the EB welds, the lower critical bound on Cr_{eq}/Ni_{eq} ratios can be expected to be between the limits for the two processes shown in Fig. 14. However, for EB welds this limit can be expected to be highly dependent upon weld solidification velocity (Refs. 12, 26). Of course, the degree of constraint also plays a critical role in solidification cracking behavior of primary austenite solidified welds.

From the mechanical property data reported here, and the weld cracking behavior summarized in Fig. 14, it can be seen a range of compositions of free-machining stainless steel exists that should provide a good combination of solidification cracking resistance, tolerance to processing procedures, and mechanical properties for many engineering applications.

Summary

The all-weld-metal tensile behavior of both GTA and EB welds exhibited similar behavior over a wide range of Cr_{eq}/Ni_{eq} ratios and sulfur contents. A slight increase in strength (~15%) with increasing calculated FN was attributed primarily to second-phase strengthening by ferrite. The wide range in sulfur, 0.04 to 0.42 wt-%, had little if any effect on strength. At the lowest Cr_{eq}/Ni_{eq} ratio of 1.55, EB weld properties were largely controlled by the presence of solidification cracks that formed during primary austenite solidification.

A strong correlation was observed between sulfur content and ductility. This was attributed to the increase in Cr- and Mn- containing sulfides with increasing sulfur content. In all cases, except in the presence of solidification cracks, fracture initiated at sulfide particles distributed mainly along solidification boundaries. The higher sulfide contents and closer sulfide spacing accelerated the ductile microvoid initiation and growth processes, and are responsible for the reduced ductility with increasing sulfur level. The decrease in RA with increasing sulfur level was somewhat more apparent in the EB welds than in the GTA welds, and this is likely associated with differences in sulfide size and spacing. The mechanical behavior of laser beam spot welds showed similar dependence with sulfur content and microstructure. Like the EB welds, solidification as ferrite minimizes the possibility of solidification cracking and is a requirement for reliable laser beam spot welds. However, it was found that at moderate sulfur levels, a good combination of strength and ductility was achieved in all three weld processes. Based on previous solidification and cracking studies on the same alloys, it was found a range of compositions of free-machining stainless steels exists that should provide a good combination of solidification cracking resistance and weld properties for many engineering applications.

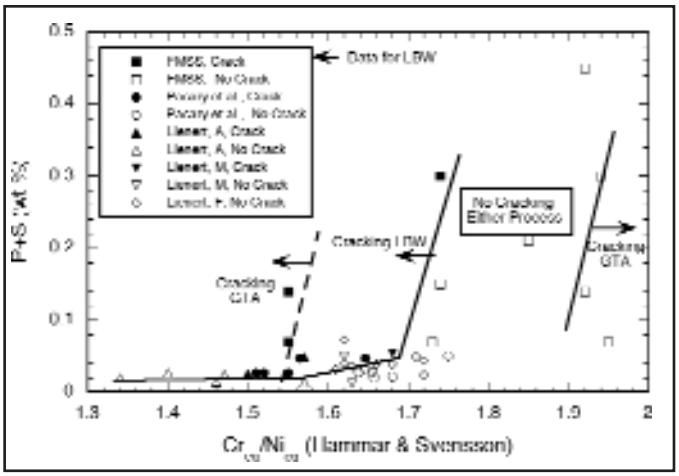

Fig. 14 — Solidification cracking susceptibility of GTA and pulsed YAG laser beam welds showing region of cracking behavior for both processes (Ref. 4 including data from Refs. 33, 34).

Acknowledgments

Special thanks is given to Andy Gardea, Jeff Chames, Alice Kilgo, and Bonnie McKenzie for metallographic services, and to Annette Newman for laboratory support on weldability testing. Appreciation is also given to Carpenter Technology Corporation for supplying the experimental alloys. This work was performed at Sandia National Laboratories, a Lockheed Martin company, for the U.S. Department of Energy under contract number DE-AC04-94AL85000.

References

1. Lundin, C. D., Lee, C. H., and Menon, R. 1988. Hot ductility and weldability of free machining austenitic stainless steel. *Welding Journal* 67(6): 122-s to 130-s.

2. Brooks, J. A., Thompson, A. W., and Williams, J. C. 1984. A fundamental study of the

beneficial effect of delta ferrite in reducing weld cracking. *Welding Journal* 63(2): 71-s to 83-s.

3. Brooks, J., Robino, C., Goods, S., Headley, T., Knorovsky, G., and Yang, N. 1999. Solidification and weldability of free machining stainless steel. *International Conference on Joining of Advanced and Specialty Materials II*. 1999 ASM Materials Solutions Conference and Exposition. Cincinnatti, Ohio: ASM International.

4. Brooks, J., Robino, C., Headley, T., and Michael, J. 2003. Weld solidification and cracking behavior of free machining stainless steel. *Welding Journal* 82(3):51-s to 64-s.

5. Hammar, O., and Svensson, U. 1979. Influence of steel composition on segregation and microstructure during solidification of austenitic stainless steels. *Solidification and Casting of Metals*. London, U. K.: pp. 401–410. The Metals Society,

6. Vitek, J. M., Dasgupta, A., and David, S. A. 1983. Microstructural modification of austenitic stainless steels by rapid solidification. *Metall. Trans. A* 14A: 1833–1841.

7. Katayama, S., and Matsunawa. 1985. Solidification microstructures of laser welded stainless steels. *Proc. ICALEO 84*. Toledo, Ohio: Laser Institute of America. pp. 60–67.

8. David, S.A., Vitek, J. M., and Hubble, T. L. 1987. Effect of rapid solidification on stainless steel microstructures and its implication on the Schaeffler diagram. *Welding Journal* 66(10): 289-s.

9. Elmer, J. W., Allen, S. M., and Eagar, T. W. 1989. Microstructural development during solidification of stainless steel alloys. *Metall. Trans.* 20A: 2117–2131.

10. Nakao, Y., Nishimoto, K., and Zhang, W. 1988. Effects of rapid solidification by laser surface melting on solidification modes and microstructure of stainless steel. *Trans. JWJI* 19:101.

11. Elmer, J. W. 1992. Non-equilibrium microstructures produced during electron-beam and laser-beam surface modification of metallic alloys. *The Metals Science of Joining*, eds. Cieslak, Perepezko, Kang, and Glicksman. Warrendale, Pa.: TMS, pp. 123–133.

12. Fukumoto, S., and Kurz, W. 1997. The δ–γ transition in Fe-Cr-Ni alloys during laser treatment. *ISIJ International* 37 (7): 677–684.

13. Borland, J. C., and Younger, R. N. 1960. Some aspects of cracking in welded Cr-Ni austenitic steels. *British Welding Journal*, Vol. 7: 22–59.

14. Brooks, J. A., and Lambert Jr., F. J. 1978. The effect of phosphorous and sulfur and ferrite content on weld cracking of type 309 stainless steel. *Welding Journal*: 51(5): 139-s.

15. Brooks, J. A. 1975. Weldability of high N, high Mn austenitic stainless steel. *Welding Journal* 54(6): 189-s to 195-s.

16. Li, L., and Messler Jr., R. W. 1999. The effect of phosphorous and sulfur on susceptibility to weld hot cracking in austenitic stainless steels. *Welding Journal* 78(12): 387-s to 396-s.

17. Kotecki, D., and Siewert, T. A. 1992. WRC-1992 constitution diagram for stainless steel weld metals: a modification to the WRC-1988 diagram. *Welding Journal* 71(5): 171-s to 179-s.

18. Long, C. J., and DeLong, W. T. 1973. The ferrite content of austenitic stainless steel weld metal. *Welding Journal* 52(7): 281-s to 297-s.

19. Suutula, N., Takalo, T., and Moisio, T. 1979. Relationship between solidification and microstructure in austenitic and austenitic-ferritic stainless steel welds. *Metall. Trans*. 10A(4): 512–514.

20. Takalo, T., Suutula, N., and Moisio, T. 1979. Austenitic solidification mode in austenitic stainless steel welds, *Metall. Trans*. 10A(4): 1173–1181.

21. Suutula, N. 1982. Effect of solidification conditions on the solidification mode in austenitic stainless steels. *Acta Universitatis Ouluensis*, Series C Technica, No. 23. Oulu, Finland: University of Oulu.

22. Brooks, J. A., and Thompson, A. W. 1991. Microstructural development and solidification cracking susceptibility of austenitic stainless steel welds. *International Materials Reviews* 36(1): 16–44.

23. Olson, D. L. 1985. Prediction of austenitic weld metal microstructure and properties. *Welding Journal* 64(11): 181-s to 295-s.

24. Brooks, J. A., Yang, N. C. Y., and Krafcik, J. S. 1992. On the origin of ferrite morphologies of primary ferrite solidified austenitic stainless steel welds. *Recent Trends In Welding Science and Technology*, eds. S. A. David and J. M. Vitek. Material Park, Ohio: ASM International. pp. 173–180.

25. Brooks, J. A., Yang, N. C. Y., and Krafcik, J. S. 2001. Clarification on the development of skeletal and lathy ferrite morphologies in stainless steel welds. *Science and Technology of Welding and Joining* 6: 412–414.

26. Suutala, N. 1982. Effect of manganese and nitrogen on the solidification mode in austenitic stainless steel welds. *Acta Universitatis Ouluensis*, Series C Technica, No. 23. Oulu, Finland: University of Oulu.

27. Goods, S. H., and Brown, L. M. 1979. The nucleation of cavities by plastic deformation. *Acta Metallurgicia* 27: 1–15.

28. Laursen, B., Olsen, F., Yardy, J., and Funder-Kristensen, T. 1997. Experimental determination of the primary solidification phase dependency on the solidification velocity of 17 different stainless steel compositions. *Proc. ASM International Conference on Welding and Joining Science and Technology*. Madrid, Spain, March 10–22: pp. 571–580.

29. Thier, H., 1976. Delta-ferrite and hot cracking during the welding of chemically resistant austenitic steels. *DVS-Berichte*, No. 41, pp. 100–104.

30. Arata, J., Matsuda, F., and Katayama, S. 1976. Fundamental investigation on solidification behavior of fully austenitic and duplex structures and effect of ferrite on microsegregation. *Trans. JWRI* 5(2): 35.

31. Masumoto, I., Tamaki, K., and Kutsuna, M. 1972. Hot cracking of austenitic stainless steel weld metal. *Trans. JWS* 41(11): 1306.

32. Lippold, J. C. 1982. Weld cracking mechanism in austenitic stainless steels. Trends in Welding Research in the U.S. *ASM Conference Proceedings*. Materials Park, Ohio: ASM International,1990. pp. 209–247.

33. Pacary, G., Moline, M., and Lippold, J. C. *EWI Research Brief No. B9008* Edison Welding Institute.

34. Lienert, T. J. 1998. A combined PSM/weldability diagram for laser welded austenitic stainless steels. *Proc. 5th Int. Conf. Trends in Welding Research*, Materials Park, Ohio: ASM International, pp. 724–728.